

Pre-visual symptoms of *Xylella fastidiosa* infection revealed in spectral plant-trait alterations

Zarco-Tejada^{1*}, P.J., Camino², C., Beck¹, P.S.A., Calderon², R., Hornero², A., Hernández-Clemente, R.³, Kattenborn⁴, T., Montes-Borrego², M., Susca⁵, L., Morelli⁶, M., Gonzalez-Dugo², V., North³, P.R.J., Landa², B.B., Boscia⁶, D., Saponari⁶, M., Navas-Cortes², J.A.

¹ European Commission (EC), Joint Research Centre (JRC), Directorate D-Sustainable Resources, Via E. Fermi 2749 – TP 261, 26a/043, I-21027 Ispra (VA), Italy

² Instituto de Agricultura Sostenible (IAS), Consejo Superior de Investigaciones Científicas (CSIC), Alameda del Obispo s/n, 14004 Córdoba, Spain

³ Department of Geography, Swansea University, SA2 8PP Swansea, United Kingdom

⁴ Institute of Geography and Geoecology, Karlsruhe Institute of Technology (KIT), Kaiserstraße 12, 76131 Karlsruhe, Germany

⁵ Dip. di Scienze del Suolo, della Pianta e degli Alimenti dell'Università di Bari, Bari, Italy

⁶ CNR, Istituto per la Protezione Sostenibile delle Piante, Bari, Italy

* *Corresponding author*

ABSTRACT

Plant pathogens cause significant losses to agricultural yields, and increasingly threaten food security¹, ecosystem integrity, and societies in general²⁻⁵. *Xylella fastidiosa* (*Xf*) is one of the most dangerous plant bacteria worldwide, causing several diseases with profound impacts on agriculture and the environment⁶. Primarily occurring in the Americas, its recent discovery in Asia and Europe demonstrates that *Xf*'s geographic range has broadened considerably, positioning *Xf* as a re-emerging global threat that has caused socio-economic and cultural damage^{7,8}. *Xf* can infect over 350 plant species worldwide⁹, and its early detection is critical for its eradication⁸. Here, we show that changes in plant functional traits retrieved from airborne imaging spectroscopy and thermography can reveal *Xf* infection in olive trees before symptoms are visible. We obtained accuracies of disease detection, confirmed by qPCR, exceeding 80% when high-resolution fluorescence quantified by 3D simulations and thermal stress indicators were coupled with photosynthetic traits sensitive to rapid pigment dynamics and degradation. Moreover, we found that the visually asymptomatic trees originally scored as affected via spectral plant trait alterations developed *Xf* symptoms at almost double the rate of the asymptomatic trees classified as not affected by remote sensing. We demonstrate that spectral plant trait alterations caused by *Xf* infection are detectable pre-visually at the landscape scale, a critical requirement to help eradicate some of the most devastating plant diseases worldwide.

Acronyms - **Anth**: Anthocyanins; **C_{a+b}**: Chlorophyll *a+b*; **C_{x+c}**: Carotenoids; **CWSI**: Crop Water Stress Index; **E**: irradiance; **Fi**: Fluorescence efficiency; **Ft**: Leaf-level steady-state fluorescence; **FP**: False Positives; **FW1**: Intensive field work 1; **FW2**: Intensive field work 2; **κ**: Kappa coefficient; **L**: radiance; **LDA**: Linear Discriminant Analysis; **NBHI**: Narrow Band Hyperspectral Indicators; **NDVI**: Normalized Difference Vegetation Index; **NIR**: Near-infrared; **NNE**: Neural Network; **NPQI**: Chlorophyll Degradation Phaeophytinization-based Spectral Trait; **OA**: Overall Accuracy; **PS**: Pigment- and Structure-based Functional Traits; **PSFT**: Pigment-Structural-Fluorescence-Temperature Plant Functional Traits; **qPCR**: Quantitative Polymerase Chain Reaction assay; **RGB**: Red-Green-Blue; **ROC**: Receiver Operating Characteristic analysis; **RT**: Radiative Transfer; **SIF**: Solar-induced Fluorescence; **SVI**: Spectral Vegetation Indices; **SVM**: Support Vector Machine; **TN**: True Negatives; **TR**: Training dataset; **TS**: Testing dataset; **V+A+Z**: Violaxanthin (V), Antheraxanthin (A), Zeaxanthin (Z) pool; **VHR**: Very-High-Resolution; **Xf**: *Xylella fastidiosa*.

51 *Xylella fastidiosa* (*Xf*) is considered one of the most dangerous plant pathogens worldwide⁶.
52 It can infect over 350 plant species⁹, causing diseases in several crops and large economic
53 losses⁸. In America, this xylem-limited plant pathogenic bacterium is associated with
54 detrimental diseases in high-value crops, such as Pierce's disease in grapevines and
55 variegated chlorosis in citrus¹⁰. Its spread has recently gained a global dimension¹¹: already
56 widely distributed in the Americas and detected in Iran and Taiwan, *Xf* has been known to
57 be present in Europe since 2013 after its official identification in Italy¹² causing economic
58 and societal damage⁸.

59

60 The spread of *Xf* within Europe has thus far not been contained⁷. Outbreaks detected in
61 France and recently in Spain have raised concerns of *Xf* spreading to the world's largest
62 olive-growing area (over 2.5 million hectares) and throughout Mediterranean agriculture⁸.
63 The identification of all three main subspecies of *Xf* (i.e., *fastidiosa*, *multiplex*, and *pauca*)
64 in Europe broadens the threat to several other crop plants, including almond, citrus, and
65 grapevine, but also to ornamental trees as well as elms, oaks and sycamores. A major
66 difficulty for *Xf* containment arises from its very wide host range, with infections that do
67 not cause symptoms in some host-strain combinations, despite the infected hosts
68 continuing to act as inoculum sources⁹. This threat is further exacerbated because *Xf* can be
69 spread via xylem-sap sucking insects without any specific vector relationship⁸, and due to
70 increased global trade.

71

72 Alarms have been raised by both the international scientific community⁸ and the media⁷,
73 pointing out that eradication of *Xf* will require robust monitoring and early detection of
74 plants that show little to no signs of decline at the early stages of infection. A major
75 limitation of standard large-scale mapping methods based on red and near-infrared (NIR)
76 (e.g. the Normalized Difference Vegetation Index [NDVI] and its multiple variations
77 obtained from broadband satellite sensors) is that they are useful only for detecting the
78 advanced stages of disease damage, i.e. when canopy defoliation, leaf wilting, and chlorosis
79 are apparent¹³. Additionally, current hyperspectral satellite sensors lack the spatial
80 resolution to distinguish individual tree crowns. Accordingly, *Xf* eradication efforts
81 involving its early detection necessitate high spatial resolution (i.e. sub-meter) imaging
82 spectroscopy and thermal data to assess subtle changes in spectral features and traits, a
83 technology that can be potentially deployed at large scales with airborne platforms¹⁴.

84

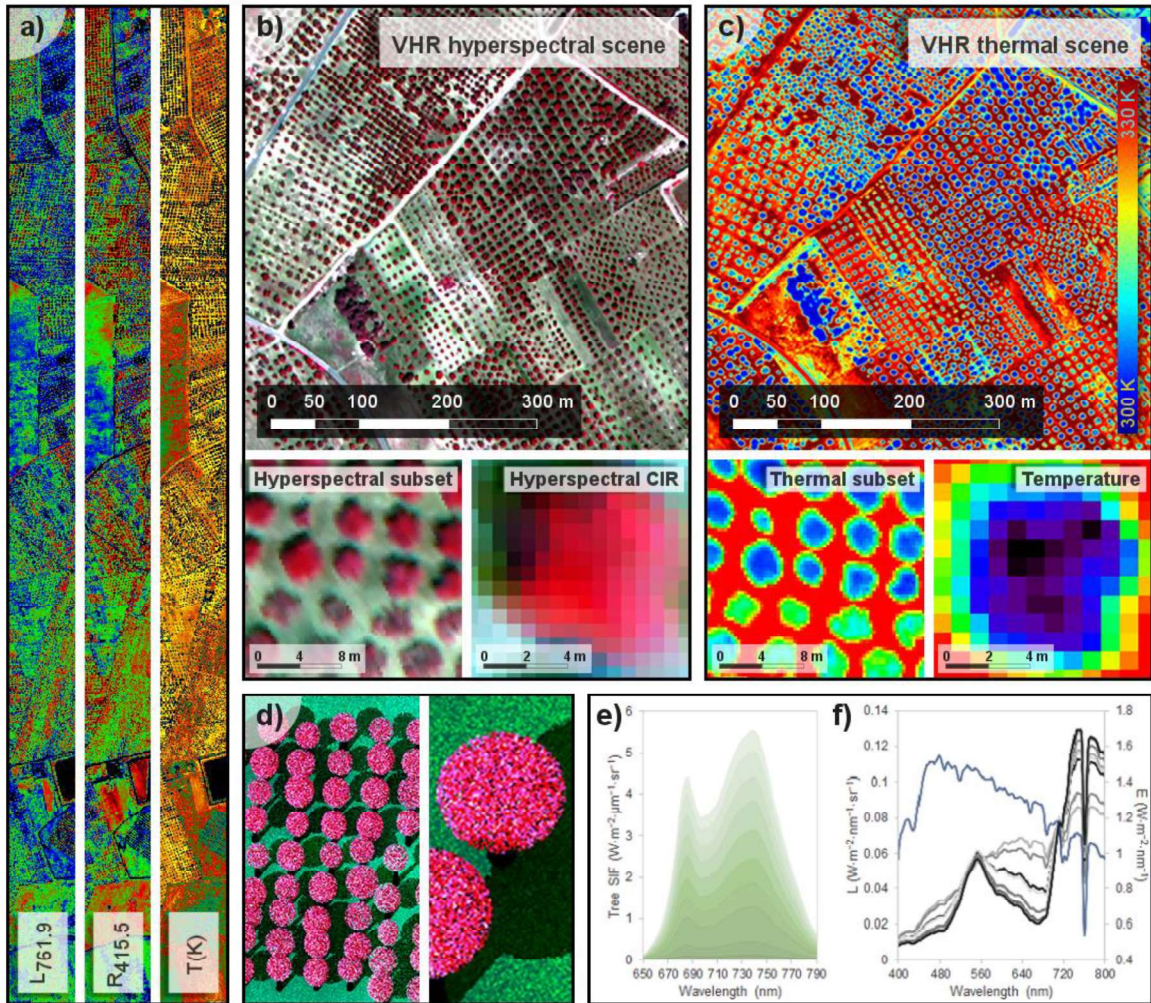
85 We carried out intensive multi-year *in-situ* inspections of >7000 trees and airborne
86 imaging data in 15 olive orchards, finding that physiological alterations caused by *Xf*
87 infection at the pre-visual stage were detectable in functional plant traits assessed remotely
88 by hyperspectral and thermal sensors. We confirmed the presence of *Xf* infection in all
89 selected orchards by testing at least two symptomatic trees per plot by quantitative
90 polymerase chain reaction assay¹⁵ (qPCR). Additionally, we sampled one of the olive fields
91 more extensively for an orchard-level validation of the remote sensing model testing, by
92 qPCR assays, 67 out of the 157 trees spanning the full range of symptoms, i.e. from
93 asymptomatic to severely affected. Although quantitative PCR is considered the most
94 sensitive diagnostic approach, its accuracy under field conditions for the detection of the *Xf*
95 in host plants is affected by the period of sampling and the uneven distribution of the
96 bacterium in the large canopy of the olive trees (especially at the early stage of infection).
97 Moreover, this type of laboratory assay is time consuming and costly, and requires skilled
98 and trained personnel. For these reasons, we evaluated non-destructive remote sensing

99 methods comprising the acquisition of spectroscopy data to build 40 cm radiance and
100 reflectance scenes in 260 narrow spectral bands (Fig. 1a;b) and in the thermal spectral
101 region (Fig. 1a;c). The entire flight campaigns covered three areas within the *Xf*-affected
102 olive growth region in Southern Italy and scanned ca. 200,000 individual trees in 2016 and
103 2017, quantifying tree-level physiology-related narrow-band spectral traits, Solar-induced
104 Fluorescence (SIF) and fluorescence efficiency (Fi) by Monte Carlo 3-D scene generation
105 (Fig. 1d) that modelled the individual tree fluorescence emissions (Fig. 1e) at the tree
106 radiance level (Fig. 1f).

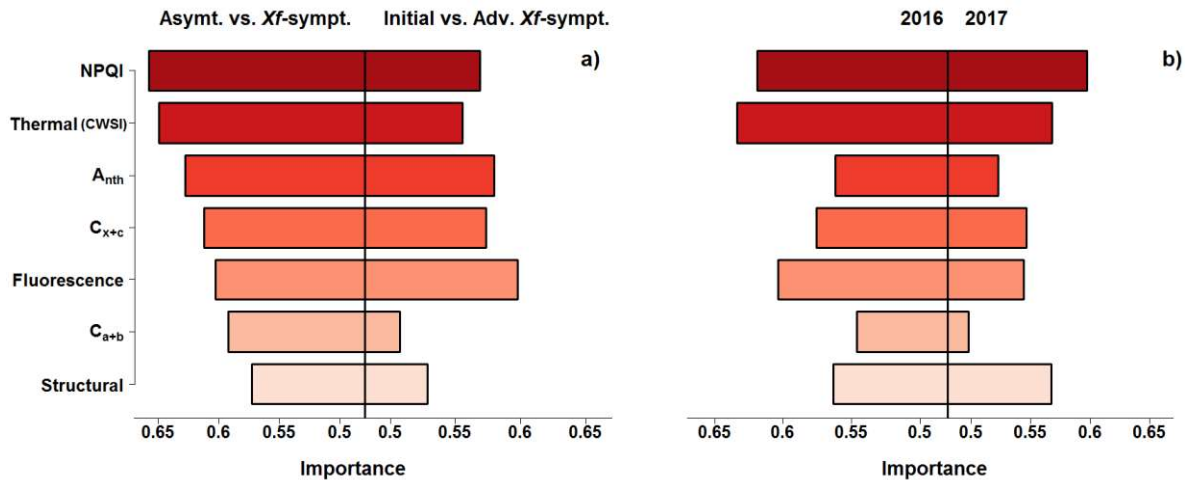
107
108 We used a multi-layered functional plant trait scheme to extract the alterations caused by *Xf*
109 from a pool of physiology-related narrow-band hyperspectral indicators (NBHI). This pool
110 included plant physiological traits specifically related to rapid changes in photosynthetic
111 pigments and leaf processes not simulated by any existing radiative transfer (RT) model,
112 e.g. the de-epoxidation state of the xanthophyll-cycle pigments via the violaxanthin (V),
113 antheraxanthin (A), and zeaxanthin (Z) pool¹⁶, and chlorophyll degradation via
114 phaeophytinization^{17,18} (see Supplementary Table 1¹³). In addition, we assessed traits
115 sensitive to *Xf* infection (i.e. anthocyanins and carotenoid / chlorophyll ratios) by a hybrid
116 wavelet-inverted model inversion method (Supplementary Table 2; Supplementary Fig. 1),
117 and quantified SIF emission and Fi by a multi-step LUT-based inversion scheme
118 (Supplementary Table 3, Supplementary Fig. 2). The inversion of radiative transfer models
119 enables the simultaneous and independent retrieval of multiple leaf and canopy traits linked
120 to physiological processes in plants. Thus, compared to single-band and index-based
121 relationships from radiance or reflectance spectra which simultaneously relate to several
122 traits (e.g. both photosynthetic pigments and structure), the model-inverted traits space is
123 more likely to reveal the physiological processes associated with the disease. Furthermore,
124 the process-based retrieval of traits by physical models increases the potential
125 transferability of findings to other data sets, diseases, and plant species. Nevertheless,
126 specific narrow-band spectral indices that track processes currently not simulated by any
127 radiative transfer simulations can complement model-estimated traits.

128
129 To reveal the gas exchange dynamics associated with *Xf* symptoms, we incorporated a
130 functional trait consisting of temperature-based plant stress indicators linked to stomatal
131 conductance and tree transpiration alterations. Linear, as well as machine- and deep-
132 learning algorithms (linear discriminant analysis, LDA; support vector machine, SVM;
133 neural network ensemble, NNE, see Methods in Extended Material) fed by the pool of
134 functional plant traits via receiver operating characteristic (ROC) analysis revealed that the
135 chlorophyll degradation phaeophytinization-based spectral trait (NPQI)^{17,18} calculated in
136 the blue region, and the thermal-based stress trait (CWSI, Crop Water Stress Index) best
137 distinguished *Xf*-symptomatic from asymptomatic trees (Fig. 2a) in both years (Fig. 2b),
138 followed by anthocyanins (A_{nth}), carotenoids (C_{x+c}) and solar-induced fluorescence.
139 Notably, the importance of the functional traits varied as a function of *Xf*-symptom
140 severity: NPQI and CWSI most reliably distinguished symptomatic from asymptomatic
141 material (Fig. 2a, left-side bars), but were of lesser importance to discriminate between
142 initial and advanced stages of the disease. For these symptomatic trees, solar-induced
143 fluorescence was the most sensitive functional trait to detect the severity of *Xf* symptoms
144 (Fig. 2a, right-side bars).

145



146 **Fig. 1. Imagery acquisition and plant-trait fluorescence retrievals.** **a**, Strips of airborne
 147 images of 40-cm hyperspectral radiance collected at the O₂-A band, reflectance at 415 nm
 148 (used to calculate NPQI), and temperature (in K). Subsets of the very-high-resolution
 149 (VHR) hyperspectral (**b**) and thermal imagery (**c**) enable the identification of single trees to
 150 extract tree-crown radiance (L), reflectance (R) and temperature. **d**, Monte Carlo simulation
 151 modelled solar-induced fluorescence (SIF) emission via 3-D scenes generated with
 152 FluorFLIGHT (**e**) from tree radiance (L) and irradiance (E) (**f**) to quantify fluorescence
 153 efficiency (Fi) by radiative transfer.

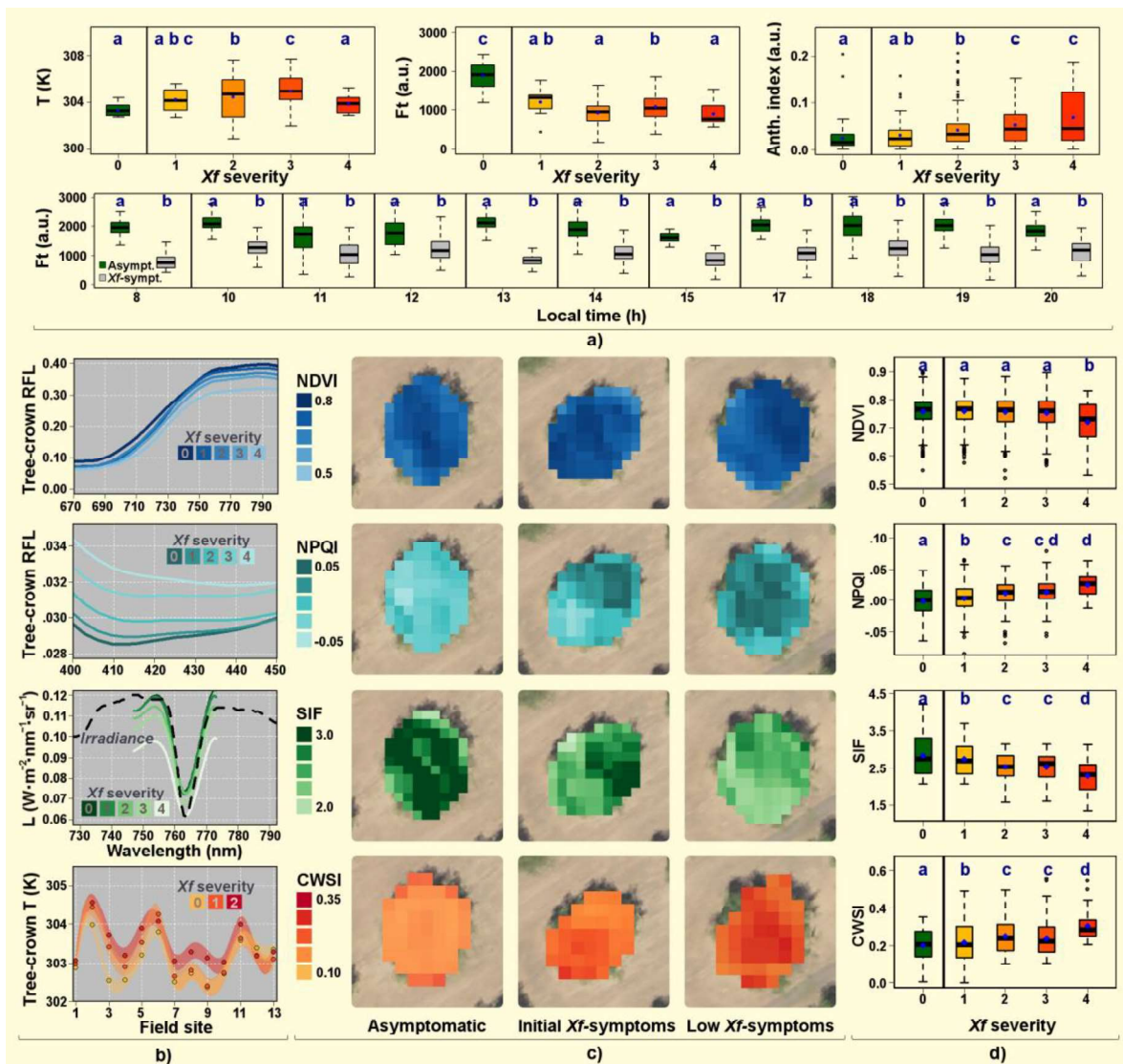


154 **Fig. 2. Contribution of remote sensing plant traits to pre-visual *Xf* symptom detection.**
 155 **a**, ROC analysis from the pool of hyperspectral and thermal plant functional traits used to
 156 detect asymptomatic vs. *Xf*-symptomatic trees (left bars) and for initial vs. advanced *Xf*-
 157 symptomatic trees (right bars). **b**, The robustness across years of the functional traits for
 158 asymptomatic vs. *Xf*-symptomatic trees. The ROC analysis was performed using the
 159 training data set (TR, n=5,852 trees).

160

161 The sensitivity of these physiology-based remote-sensed plant traits to pre-visual and early
 162 stages of the *Xf*-infection is supported in the literature by work that shows the
 163 photoprotective role of carotenoids (C_{x+c}) and the protection from damage induced by
 164 environmental stresses and plant pathogens provided by flavonoids such as anthocyanins
 165 (A_{nth})¹⁹. These compounds accumulate in *Xf*-infected plant material²⁰ and are produced by
 166 the degradation of the chlorophyll molecule into phaeophytin under stress conditions^{17,18}. In
 167 addition, the alterations in stomatal regulation²¹ and photosynthesis caused by plant-
 168 pathogen interactions²² lead to decreased fluorescence^{13,23} and transpiration²⁴, and produce
 169 phenolic plant-defense compounds²⁵.

170 The alterations of plant functional traits we detected remotely were highly consistent with
 171 *Xf*-induced leaf physiological changes measured *in-situ*. In particular, the changes we
 172 observed in the *in-situ* A_{nth} , steady-state fluorescence Ft, and temperature leaf traits (Fig.
 173 3a; Supplementary Fig. 3) were in line with the alterations observed in the corresponding
 174 traits quantified from the imagery, such as A_{nth} (Supplementary Fig. 1), SIF and CWSI
 175 (Fig. 3d). These traits differed significantly between asymptomatic and symptomatic
 176 leaves, even when symptoms were mild (Tukey's HSD test, $P < 0.05$) (Supplementary Fig.
 177 3). Moreover, the high-resolution images revealed between- and within-tree-crown patterns
 178 of the functional traits associated with *Xf* infection (Fig. 3b;c). Although widely used in
 179 global monitoring of vegetation, NDVI did not differ significantly between asymptomatic
 180 and symptomatic trees (Fig. 3d), and was therefore unable to detect non-visual symptoms
 181 of *Xf* infection. We found that the reflectance changes in the blue region consistently
 182 tracked early and initial *Xf* symptoms, in particular the 415 and 435 nm spectral bands used
 183 to calculate the chlorophyll degradation phaeophytinization-based spectral trait NPQI^{17,18},
 184 which was the NBHI indicator most sensitive to *Xf* infection. The SIF calculated from the
 185 airborne radiance imagery and CWSI calculated from the remotely sensed tree crown
 186 temperature, showed statistically-significant ($P < 0.001$) and consistent trends for early *Xf*
 187 symptoms.



188 **Fig. 3. Relationships between remote-sensed functional plant traits and *Xf* disease severity levels at leaf and canopy levels.** **a**, Temperature (T, n=922 leaves), fluorescence
189 (Ft, n=1,197 leaves) and anthocyanins (A_{nth} , n=939 leaves), as well as hourly Ft (n=2,863
190 leaves), measured in asymptomatic (*Xf* severity = 0) and increasingly symptomatic leaves
191 of *Xf*-infected olive trees. **b**, Mean tree-crown reflectance for trees with increasing severity
192 of *Xf* symptoms in the red-NIR region (n=923 trees), blue region (n=923 trees), O₂-A
193 radiance region for SIF quantification (n=923 trees), and temperature (n=1,493 trees). The
194 standard deviation for the tree-crown T data is represented as shaded. **c**, Respective
195 associated maps of NDVI, NPQI, SIF and CWSI, showing the within-crown variation of
196 traits in asymptomatic, initial, and low *Xf*-symptomatic trees. **d**, Trait values across the
197 entire sample of trees for NDVI, NPQI and SIF (n=1,493 trees) and CWSI (n=1,446 trees).
198 The disease severity at leaf and canopy levels was compared by one-sided Tukey's HSD
199 test at 5%. Severity levels with same letter are not significantly different (Tukey HSD test,
200 *p*-value <0.05). In the box plots, the black line represents the median, and the top and
201 bottom are the 75th and 25th quartiles. The whiskers are the upper and lower limits based on
202 the interquartile ranges ($Q \pm 1.5 \times IQR$). Average values are shown with a blue point. The
203 outliers (circles), are the values out of the upper and lower limits. a.u.: arbitrary units.A
204

205 pool of plant functional traits comprising pigment and structural traits, together with a flux-
206 based fluorescence trait and temperature (PSFT) obtained the best overall accuracy (OA)
207 and kappa coefficient (κ) for *Xf* detection through the SVM algorithm, yielding OA =
208 80.9% and $\kappa = 0.61$ (Fig. 4a; Supplementary Tables 4 and 5). By contrast, models built
209 without SIF and temperature traits (i.e. the Pigment- and Structure-based Functional Traits,
210 PS model), and particularly one limited to standard red-green-blue (RGB)-NIR spectral
211 vegetation indices (SVI) commonly found in satellite sensors (NDVI, and blue / green / red
212 ratios; SVI model), obtained the lowest accuracies (OA=65.4%; $\kappa=0.29$). We obtained
213 these results through validation with visual inspection data collected by plant pathologists
214 from 1,332 trees per year in 15 fields, generating a large dataset with statistical robustness
215 and ample variability in disease severity levels, tree structure and age, and agronomic
216 management of the orchards within the *Xf*-infested zone.

217
218 We evaluated the accuracies of the remote sensing-based SVM-PSFT disease detection
219 model and the visual inspections using quantitative PCR assay data obtained in a selected
220 olive orchard. The assessment of the orchard-level remote sensing model validated with the
221 tree-level qPCR dataset yielded OA=94.03% and $\kappa=0.88$. The performance of the visual
222 inspection against qPCR (OA=77.62% and $\kappa=0.55$) showed the validity of the evaluations
223 by the plant pathologists, but reflected a lower performance than that using remote sensing
224 methods due to the impossibility of visually detecting the asymptomatic infections that
225 were detected by qPCR. The validation of the remote-sensing model with qPCR data
226 enabled the generation of a spatial map of disease incidence prediction by remote sensing,
227 revealing infected asymptomatic trees that were missed by the visual evaluations (Fig. 5a)
228 but detected by remote sensing (Fig. 5b). Among all trees measured in this particular
229 orchard by qPCR (n=67), those visually considered asymptomatic by plant pathologists
230 (n=40) but proven infected via qPCR (n=11) were detected as infected by remote sensing
231 with 91% accuracy. When the analysis was extended to eight orchards where the
232 qPCR-sampled trees were visible in the imagery (n=100), the accuracy of the remote
233 sensing model validated with the tree-level qPCR dataset yielded OA=96% and $\kappa=0.92$,
234 whereas the performance of the visual inspection against qPCR remained at the same level
235 as the orchard-level analysis (OA=77% and $\kappa=0.54$). Moreover, the remote sensing
236 SVM-PSFT model detected 92.9% of the infected asymptomatic trees (qPCR=1; DS=0)
237 that were missed by visual assessment (Supplementary Table 6).

238
239 These results obtained by remote sensing and validated with qPCR data suggested the
240 existence of trees in the very early stage of the disease that were missed by the visual
241 evaluations. To explore whether our remote sensing model fed by plant functional traits
242 actually detected the early symptoms at a pre-visual stage, a temporal dimension was added
243 in the analysis. Indeed, a critical finding of this study arose from further investigation of the
244 trees seemingly wrongly considered symptomatic by remote sensing (i.e. those initially
245 considered ‘false positives’ based on examination by plant physiologists) over the course of
246 two years through periodic field revisits. False-positive cases may arise from: i) error and
247 uncertainty inherent to the remote sensing model used for detecting affected trees; and ii)
248 trees that were indeed affected by *Xf* but did not yet display the typical visible symptoms
249 upon which plant pathologists rely. Thus, we revisited *in situ* (Fig. 4b; Supplementary
250 Table 7) the trees identified as symptomatic by the remote-sensing plant functional trait
251 model applied to the 2016 image data (F1) but classified at the time as asymptomatic by

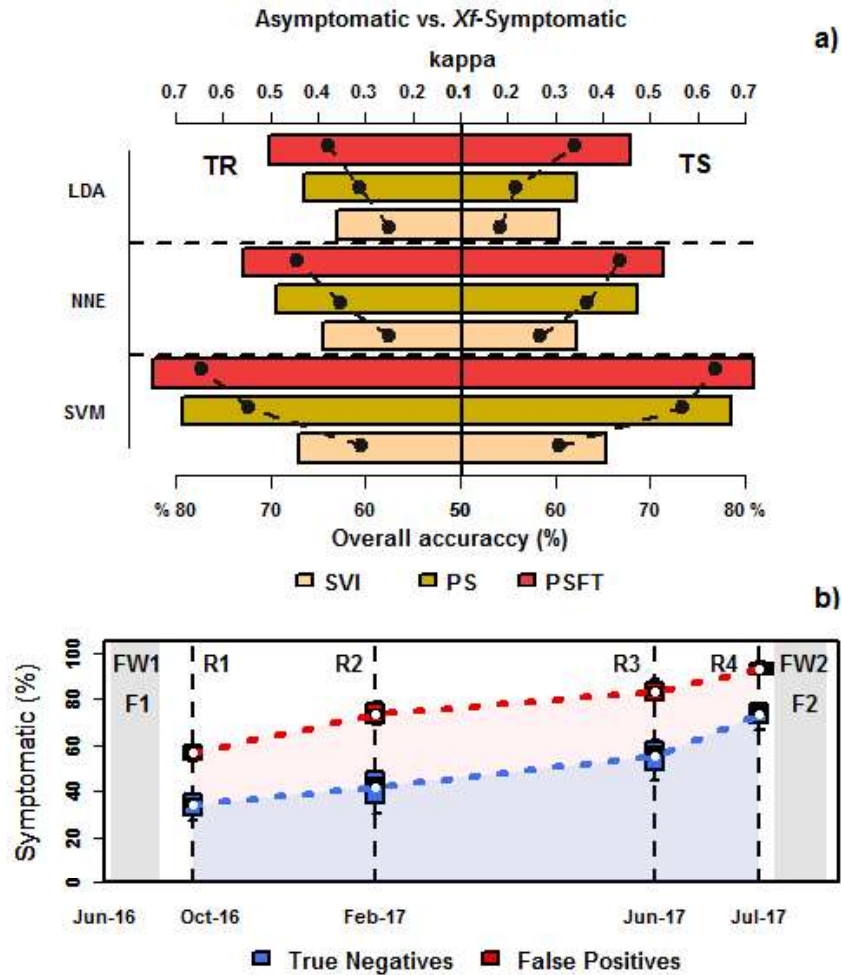
252 plant pathologists based on the absence of visible symptoms (false positives, FP; n=178 by
253 SVM).

254

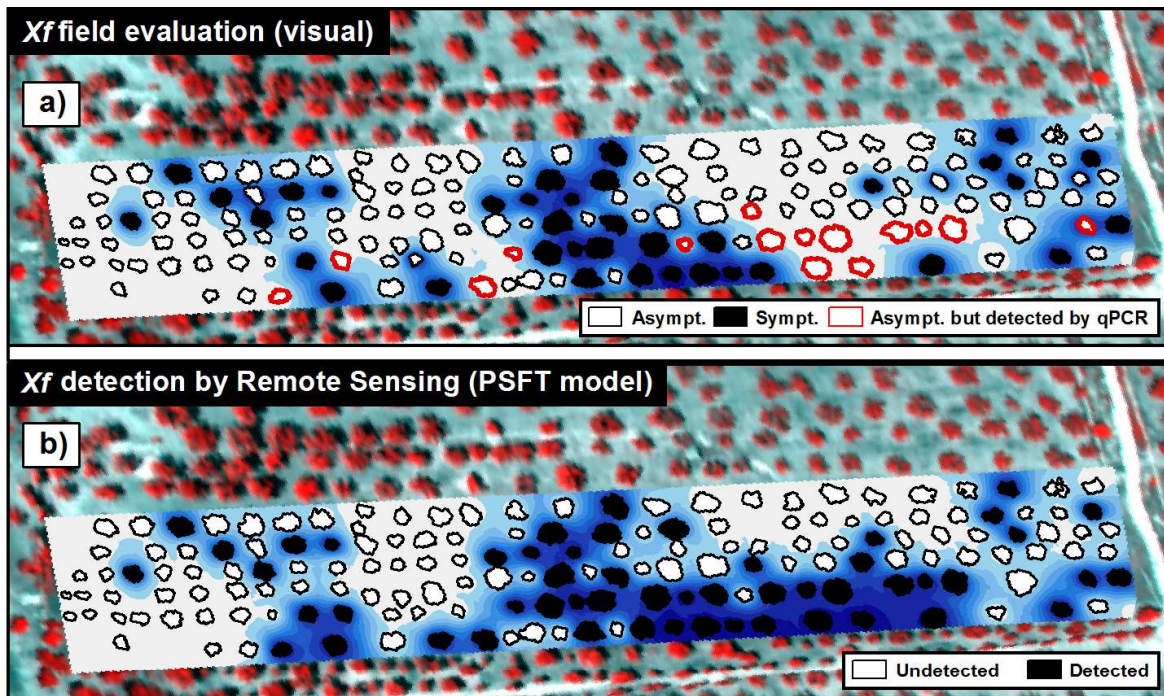
255 During these field revisits conducted four (indicated as R1), eight (R2), eleven (R3), and
256 twelve months (R4) after the flight at the F1 date, we recorded the development of visible
257 *Xf* symptoms on 1,700 out of the 3,328 trees initially evaluated. Four months after F1, 61%
258 of the false positives had developed symptoms, while only 39% of the asymptomatic trees
259 classified as unaffected by the remote sensing-driven PSFT model had (true negatives, TN,
260 n=818, two-sided t-test: $P < 0.001$). This difference in visible symptom development was
261 maintained throughout the one-year post-flight evaluations (R1, R2, R3 and R4), with FP
262 trees consistently developing symptoms sooner than TN trees. These results obtained in the
263 multitemporal revisit scheme and via qPCR confirmed that the remote sensing-driven PSFT
264 model based on plant functional traits was able to detect *Xf* symptoms earlier than standard
265 visual inspections by plant pathologists. The ability to detect pre-visual infections is
266 particularly relevant given the threat of infected but asymptomatic trees contributing to the
267 *Xf* epidemics, as plants artificially infected with *Xf* and maintained in controlled
268 environmental conditions take 10 to 12 months to start developing visible symptoms^{8,12}.

269

270 Notably, our analysis was not based just on single spectral bands or indices to feed the
271 model. Instead, we used radiative-transfer to independently quantify physiological traits
272 linked to photosynthesis, pigment degradation, and structural changes of trees undergoing
273 early stress caused by *Xf* infection. This methodology permits generalization and transfer to
274 other plant species or diseases, since the retrieved traits are closely or even directly linked
275 to the physiological changes occurring in affected vegetation. The relative importance of
276 these traits for disease detection will differ among pathogens and host plants, depending on
277 the physiological effects associated with the disease. Operational remote-sensing based
278 detections of pathogen infections should thus rely on the spectral bandsets enabling the
279 retrieval of the most sensitive plant traits linked with a particular disease. In our case,
280 aircraft payloads imaging <10 narrow bands (e.g. 10 nm or less) in the visible-near infrared
281 region in tandem with a broad-band thermal sensor would reach overall accuracies
282 exceeding 70%. As global trade increasingly exposes natural and agricultural systems to
283 exotic pathogens, such advanced large-scale physiology-focused remote sensing methods
284 relying on plant functional traits could prove critical to prevent and manage plant disease
285 epidemics worldwide.



286 **Fig. 4. Remote sensing model performance and re-visit analysis results.** **a,** Overall
 287 accuracy (bars) and kappa coefficient (κ , bullets) of linear discriminant analysis (LDA),
 288 neural network (NNE) and support vector machine (SVM) algorithms distinguishing
 289 asymptomatic from *Xf*-symptomatic trees using as inputs standard vegetation indices
 290 calculated from RGB-NIR bands (SVI), Pigment- and Structure-based Functional Traits
 291 (PS), and Pigment-, Structure-, Fluorescence and Temperature-based Functional Traits
 292 (PSFT). Statistics are shown separately for the data ($n=7,315$ trees) used in training (TR,
 293 $n=5,852$ trees) and testing (TS, $n=1,463$ trees) for each of the three algorithms. **b,** Fraction
 294 of trees that were asymptomatic in June 2016 but showed visible symptoms during later
 295 revisits, for trees classified as non-symptomatic ($n=818$ trees for SVM, $n=588$ trees for NN
 296 and $n=534$ trees for LDA) and symptomatic ($n=178$ trees for SVM, $n=408$ trees for NN
 297 and $n=462$ trees for LDA) by remote sensing (true negatives, TN, and false positives, FP,
 298 respectively). F1 and F2 indicate the dates of the airborne imaging campaigns, which
 299 corresponded with intensive field work (FW1 and FW2). The field revisits conducted are
 300 indicated as R1, R2, R3 and R4. The dotted blue and red lines represent the cumulative sum
 301 of the fraction of trees that were identified as TN and FP by the three algorithms. In the box
 302 plots, the black line within the box represents the median of the predictions of the three
 303 algorithms, and the top and bottom of the box are the 75th and 25th quartiles, respectively.
 304 The whiskers represent the upper and lower limits based on the difference with the
 305 interquartile ranges ($Q \pm 1.5 \times IQR$). The average percentage predicted by the three
 306 algorithms is shown with a white point within the boxplot.



307 **Fig. 5. Field evaluation, qPCR tests and remote sensing spatial predictions.** **a**, Map of
 308 an olive orchard imaged by thermal and hyperspectral remote sensing showing the visual
 309 evaluation by plant pathologists in the field. **b**, Remote sensing PSFT model used to detect
 310 *Xf*-affected trees. The visually asymptomatic trees assessed as affected by qPCR (shown
 311 with red border) in (a) and therefore missed in the field evaluations by plant pathologists
 312 were detected by remote sensing using functional traits (b) with 91% accuracy. Background
 313 in stronger blue tones shows the areas more affected by *Xf*.

314
 315
 316

317 **Methods**

318

319 **Field data collection.** We assessed incidence and disease severity (DS) of *Xf*-induced
 320 symptoms in the field in June 2016 and July 2017 in 15 orchards in the *Xf*-infected area of
 321 Puglia, Southern Italy. Planting density and overall orchard management were highly
 322 variable within the selected area. We evaluated DS by visually inspecting every tree for
 323 symptoms of canopy desiccation and assessing it on a 0–4 rating scale according to the
 324 percentage of canopy affected by the disease symptoms; 0 indicated the absence of visually
 325 detectable symptoms (asymptomatic) and 4 referred to trees showing canopies with a
 326 prevalence of dead branches. In total, we evaluated 3,328 trees in 2016 [1,442 (DS = 0),
 327 762 (DS = 1), 802 (DS = 2), 250 (DS = 3), and 72 (DS = 4)] and 3,987 trees in 2017 [2,607
 328 (DS = 0), 687 (DS = 1), 555 (DS = 2), 122 (DS = 3), and 15 (DS = 4)]. Most of the olive
 329 orchards sampled had old trees (>50 years old) of cultivars Ogliarola Salentina and Cellina
 330 di Nardò, the native and widespread cultivars in the area. These cultivars have been shown
 331 to be highly susceptible to the CoDiRO strain associated with the Italian *Xf* epidemic. *Xf*-
 332 infected trees of both cultivars typically show severe desiccation that rapidly encompasses
 333 the entire canopy (within 2–3 years), and causes complete canopy die-back. Only one olive
 334 orchard consisted of trees of the Leccino cultivar (ca. 35 years old), which has genetic traits

335 of resistance to *Xf*, as demonstrated by the lower bacterial concentrations in trees of this
336 cultivar and the milder symptoms in infected trees²⁶.

337

338 During the field campaigns, we conducted different physiological measurements on leaves
339 (Fig. 3a; Supplementary Fig. 3). Flavonoid (FLAV) concentration, chlorophyll content,
340 anthocyanin content index, nitrogen balance index (NBI), and leaf temperature were
341 measured on 15/25 asymptomatic/symptomatic leaves per tree using a leaf clip Dualex 4
342 (Force-A, Orsay, France). On the same leaves, the steady-state leaf fluorescence yield (Ft)
343 and the leaf reflectance within the visible and near-infrared regions were measured with a
344 FluorPen FP100 and PolyPen RP400, respectively (Photon Systems Instruments, Brno,
345 Czech Republic), calculating leaf NPQI. We conducted a revisit assessment of disease
346 severity in October 2016 and February, June, and July of 2017, re-evaluating 1,700 of the
347 3,328 trees originally evaluated in June 2016. In the 15 olive orchards selected for
348 symptom scoring, we confirmed the presence of *Xf* infections by sampling and testing at
349 least two symptomatic trees per plot. Diagnostic tests were performed using a quantitative
350 PCR (qPCR) assays¹⁵ in all orchards under study. In addition, one of the orchards was
351 selected for a more extensive testing by qPCR assay, using 67 out of the 157 trees of this
352 orchard. This qPCR dataset was used to validate the remote sensing and the visual
353 evaluation methods. Based on the qPCR assays, the trees were categorized as positive
354 (presence of infection) or negative (no bacterial infection detected) based on the resultant
355 quantification cycle (Cq) values. Clear-cut values were consistently obtained for the trees,
356 both symptomatic and asymptomatic, categorized as qPCR-positive (i.e. Cq ranging from
357 23 to 28; a positive result is considered if $Cq < 35$ and a clear exponential fluorescence
358 curve is observed). Conversely, no fluorescence ($Cq=0$) was detected in the trees
359 categorized as qPCR-negative. We used the data from eight orchards where the
360 qPCR-sampled trees were visible in the imagery ($n=100$) for further statistical analysis. In
361 particular, we evaluated the detection by the SVM-PSFT remote sensing model of the
362 *Xf*-infected trees ($n=58$), splitting them into infected symptomatic (qPCR=1; $DS \geq 1$; $n=44$)
363 and infected asymptomatic trees (qPCR=1; $DS=0$; $n=14$) as assessed by qPCR in the
364 laboratory.

365

366 **Hyperspectral and thermal image data collection and processing.** We acquired imagery
367 on 28 June 2016 and 5 July 2017 over 1,200 ha within the *Xf*-infected area using a
368 hyperspectral sensor and a thermal camera on board a manned aircraft. Both cameras were
369 flown 500 m above ground level (AGL) at midday, acquiring hyperspectral and thermal
370 imagery at 40 cm and 60 cm pixel resolution, respectively. We covered the visible and
371 near-infrared regions with a micro-hyperspectral imager (VNIR model, Headwall
372 Photonics, Fitchburg, MA, USA) operating in the spectral mode of 260 bands acquired at
373 1.85 nm/pixel and 12-bit radiometric resolution, yielding 6.4 nm full-width at half-
374 maximum (FWHM) with a 25-micron slit in the 400–885 nm region. We set the frame
375 storage rate on board the aircraft to 50 frames per second with 18 ms integration time. The
376 8-mm focal length lens yielded an instantaneous field of view (IFOV) of 0.93 mrad and an
377 angular field of view (FOV) of 49.82°. We calibrated the hyperspectral sensor
378 radiometrically in the laboratory with an integrating sphere (CSTM-USS-2000C Uniform
379 Source System, LabSphere, North Sutton, NH, USA) using coefficients derived from a
380 calibrated uniform light source at four illumination and six integration times. Atmospheric
381 correction enabled the conversion of radiance values to reflectance using total incoming
382 irradiance simulated with the SMARTS model^{27,28}. In addition, we measured aerosol

383 optical depth in the field at 550 nm with a Micro-Tops II Sunphotometer model 540 (Solar
384 LIGHT Co., Philadelphia, PA, USA) during the flight. We ortho-rectified the hyperspectral
385 imagery with PARGE (ReSe Applications Schl pfer, Wil, Switzerland), using inputs from
386 an inertial measuring unit (IMU) (IG500 model, SBG Systems, France) installed onboard
387 and synchronized with the micro-hyperspectral imager. Due to the high spatial resolution
388 collected (40 cm) and the large size of most of the trees studied (>5 m) spatial binning was
389 applied to increase the signal-to-noise ratio (SNR) of the instrument. In addition, we
390 applied spectral binning due to the large number of spectral bands collected with
391 oversampling (260 bands @ 1.85 nm sampling interval). After performing both spatial and
392 spectral binning, SNR increased to values >300:1, showing radiance spectra with absence
393 of noise (Fig. 1f) and in the reflectance spectra (Fig. 3b). The thermal camera (FLIR
394 SC655, FLIR Systems, USA) had a resolution of 640×480 pixels and was equipped with a
395 24.6 mm f/1.0 lens connected to a computer via the GigaE protocol. This camera has a
396 spectral response in the range of 7.5-14 µm and operates with a thermoelectric cooling
397 stabilization, yielding high sensitivity below 50 mK. We calibrated the camera in the
398 laboratory using a blackbody (model P80P, Land Instruments, Dronfield, UK) at varying
399 target and ambient temperatures, and in the field through vicarious calibrations using
400 surface temperature measurements obtained following Calderon *et al.*¹³.

401

402 The high-resolution hyperspectral and thermal imagery acquired over the orchard allowed
403 single-tree identification using automatic object-based crown detection algorithms. The
404 algorithms were used to calculate mean temperature and hyperspectral reflectance for pure
405 crowns. We used image segmentation procedures as described in Calder n *et al.*²⁹. In this
406 study, we applied four image segmentation methods to the thermal and hyperspectral
407 images to extract temperature, radiance, and reflectance spectra from each pure tree crown.
408 The very high-resolution imagery acquired enabled the identification and delineation of
409 each tree crown independently in the thermal and hyperspectral datasets, minimizing
410 background and within-crown shadow effects at the border pixels of each tree crown. The
411 object-based image segmentation methods selected for the results reported here were
412 Niblack’s thresholding method³⁰ and Sauvola’s binarization techniques³¹ to separate tree
413 crowns from the background. Next, we applied a binary watershed analysis using the
414 Euclidean distance map for each object³² to automatically separate trees with overlapping
415 crowns. We calculated narrow-band spectral indices for each tree crown from the 260
416 spectral bands extracted by image segmentation. The spectral index-based traits explored in
417 this study are closely related to specific features of leaf physiology, and therefore
418 potentially sensitive predictors of the disease¹³. Thus, according to the effects of *Xf*
419 infection in olive trees, we selected spectral indices from the plant-trait functional groups
420 related to chlorophyll, carotene and xanthophyll pigments.

421

422 **Model inversion methods.** The derivation of canopy structural parameters and leaf
423 biochemical constituents from each individual tree was performed by inversion of the
424 radiative transfer model PROSAIL for the pure-vegetation pixels extracted from each tree
425 crown. The model couples the leaf reflectance PROSPECT model, accounting for leaf
426 properties such as pigment concentrations, and the canopy reflectance model SAIL, which
427 accounts for canopy structural properties, such as leaf inclination and the sun-observer
428 geometry. The versions used in the present study were PROSPECT-D³³ and 4SAIL³⁴,
429 respectively. The inversion of PROSAIL was performed using a Look-up-Table (LUT)
430 approach, in which randomized input parameters (Supplementary Table 2) are used to

431 simulate canopy reflectance data, which was then compared to the acquired airborne
432 spectra. To reduce the complexity and thus alleviate the ill-posed problem of the LUT
433 inversion, we fixed several parameters by assuming that their variation is relatively low for
434 the canopies under investigation or that the spectral range considered (400-885 nm) is not
435 affected by these parameters. The variable parameters considered comprised chlorophyll
436 content, carotenoid content, anthocyanin content, mesophyll structure, leaf area index and
437 the average leaf angle. For the LUT generation, the values for these parameters were
438 sampled from a uniform distribution within a range that is plausible for the assessed plant
439 canopies (Supplementary Table 2). Previous studies demonstrated that wavelet analysis
440 improved radiative transfer model inversions³⁵⁻³⁷. It decomposes the reflectance spectra
441 into frequency components of different scales and thus spectral characteristics, such as
442 absorption features of plant pigments. Accordingly, the correspondence in terms of RMSE
443 between simulated spectra and airborne spectra was measured using a transformation of the
444 reflectance spectra into 6 continuous wavelets derived by a Gaussian kernel. The estimates
445 for each trait were derived by selecting the 1% of the LUT entries and respective spectra
446 that resulted in the smallest RMSE. The parameter values of these LUT entries were
447 subsequently weighted by their RMSE and averaged. A summary of the traits retrieved for
448 each severity level is given in Supplementary Fig. 1.

449

450 We retrieved sun-induced chlorophyll fluorescence (SIF) emission throughout the leaf and
451 canopy using the 3-D model FluorFLIGHT³⁸. The model is based on existing theory of
452 radiative transfer by coupling the leaf fluorescence model FLUSPECT³⁹ and the 3-D ray-
453 tracing model FLIGHT^{40,41} to account for the canopy components. Input data required to
454 run the models are described in Supplementary Table 3. FluorFlight was used to i) estimate
455 F_i independently from other confounding factors (LAI, C_{a+b}), and ii) to evaluate the F_i
456 estimation from the O_2 -A *in-filling* FLD method with a 6.4 nm FWHM sensor. We used
457 FluorFLIGHT in a multi-step LUT-based inversion scheme³⁸ to retrieve full crown SIF and
458 F_i from a complex scene accounting for the influence of scene structure and composition.
459 F_i was quantified based on the FLD2 calculation from the airborne image using the LUT
460 derived from FluorFLIGHT. As a prior step, we quantified the optimal parameter
461 combination of N, C_{a+b} , C_{x+c} and LAI using PROSAIL^{42,43}. The model was originally
462 developed at 1 nm FWHM. For comparisons with the airborne hyperspectral imagery, we
463 used model simulations convolved to 6.5 nm FWHM to match the spectral resolution of the
464 radiance imagery acquired by the hyperspectral airborne sensor, evaluating the effects of
465 the bandwidth on the F_i vs. SIF relationship (Supplementary Fig. 2).

466

467 **Statistical analysis.** We used multivariate analyses based on classification and machine
468 learning algorithms to classify disease incidence and severity. We assessed the ability of
469 various selections of spectral indices to estimate disease severity (DS) using support vector
470 machine (SVM), neural networks (NN) and linear discriminant analysis (LDA). We tested
471 these modelling approaches for three different objectives, assessing the separation between:
472 (i) Case A: asymptomatic (AS) vs. symptomatic trees (AF; affected), and (ii) Case B: Initial
473 Xf -symptoms (IN, DS=1) vs. advanced Xf -symptoms (AD, DS = 2, 3, and 4) severity levels.
474 We validated the selected models by partitioning the data set into two samples: the training
475 sample (TR), containing 80% of the data collected over two years (2016 and 2017) for each
476 disease severity class selected at random, and the testing or validation sample (TS), with the
477 remaining 20%. We fitted each model using the training sample and validated it by using
478 the testing sample to assess its classification accuracy. In a first step, we performed a

479 variable reduction based on variance inflation factor (VIF) analysis for each of the two
480 objectives described (Cases A and B) on the training set. This was done to avoid
481 multicollinearity among predictor variables (i.e. plant traits). The variables with a VIF
482 lower than 10 were retained for model development. Variables used to build the different
483 models evaluated were i) single reflectance bands, for operational purposes we assessed the
484 10 most sensitive wavelengths related to the disease; ii) spectral indices listed in
485 Supplementary Table 1, with which we found the indices most sensitive to the disease to be
486 NPQI, CWSI, PRI-CI, PRIn SIF, BF1, PRIM1, CRI700m, BF2, PRIM4, DCabxc, VOG2,
487 and TCARI/OSAVI; and iii) plant traits estimated by model inversion (Fig. 2) using the
488 radiative transfer models indicated above. Wilks' lambda method⁴⁴ was used to identify the
489 variables with the greatest contribution. Then, we used the data retained through VIF
490 analysis in the three classification methods (SVM, NN and LDA). We performed the SVM
491 analysis using R software (version 3.4.0; R Development Core Team, Vienna, Austria) with
492 the "e1071" package⁴⁵. We applied a non-linear SVM classification method using the radial
493 basis function kernel. We built the NN using the "nnet" package⁴⁶ in R, based on feed-
494 forward networks with a single hidden layer. To reach the best performance of the NN,
495 guaranteeing the maximization of its algorithm, we trained 500 NNs for each objective and
496 selected the one with the highest classification accuracy. In addition, we set the NN
497 parameter size, the number of units in the hidden layer, and the weight decay for the
498 quantification of the penalty of misclassification errors using a cross-validation approach
499 within the "caret" package⁴⁷ in R. We also conducted LDA using the "caret" package in R
500 to generate a discriminant function capable of determining the classification accuracy of the
501 dataset, based on the pooled covariance matrix and the prior probabilities of the
502 classification groups⁴⁴. We assessed the classification accuracies of three different sets of
503 plant traits: 1) Pigment-, Structure-, Fluorescence and Temperature-based Functional Traits
504 (PSFT); 2) Pigment- and Structure-based Functional Traits (PS); and 3) Standard RGB-NIR
505 bandset (SVI) by calculating the overall accuracy (OA, in %) and the kappa coefficient (κ),
506 which provides an overall accuracy assessment for the classification based on commission
507 and omission errors for all classes⁴⁸.

508
509 We applied non-linear SVM classification models using the radial basis function with a
510 leave one out cross validation (LOOCV) and a stochastic gradient boosting machine to test
511 the remote sensing-based PSFT model with qPCR assay data obtained in: i) one field with
512 trees affected by *Xf* and asymptomatic trees (n = 67 trees tested; total number of trees in the
513 orchard = 157); and ii) trees tested with qPCR (n=100) located within eight olive orchards
514 throughout the study area. Training of the SVM model was performed using an iterative
515 procedure implemented with the "caret" package⁴⁷ in R. In a first step, balance techniques
516 were performed to minimize unbalanced data effects; then, we conducted 50 iterations of
517 non-linear SVM classification methods to predict the quantitative PCR data using the using
518 the remote sensing-based PSFT model. In the next step, a sequential stochastic gradient
519 boosting was trained using an ensemble model obtained from 50 SVM predictions. We
520 fitted each non-linear SVM model and ensemble model to assess its classification accuracy.
521 We assessed the classification accuracies of the proposed remote sensing SVM-PSFT
522 disease detection model and the visual evaluation performed by plant pathologists against
523 qPCR assay data obtained at the orchard level.

524
525 In October 2016, February, June, and July 2017 we revisited 1,700 out of the 3,328 trees
526 evaluated in June 2016 to assess the potential of the remote sensing-based methods to

527 detect trees affected by *Xf* before symptoms become visible. We selected the revisited plots
528 to cover a wide range of initial disease incidence and severity values. The revisit study
529 focused on calculating the confusion matrix for each model to predict disease severity for
530 the trees evaluated in June and re-evaluated in October 2016. We used this confusion
531 matrix to calculate the percentage of true negatives (TN, i.e. trees classified as
532 asymptomatic by remote sensing and field assessment in June) and false positives (FP, i.e.
533 trees classified as symptomatic by remote sensing but showing no visual symptoms in the
534 field assessment in June) that developed symptoms in October. In total, the 1700 evaluated
535 trees in the revisit consisted of 818 (TN), 412 (True Positives, TP), 178 (FP), and 292
536 (False Negatives, FN). The results for the studied cases (A, B) and all classification
537 methods (SVM, NN, and LDA) are shown in Supplementary Tables 4 and 5, the results of
538 the qPCR data analysis across eight orchards are shown in Supplementary Table 6, and the
539 revisit study for the SVM method is displayed in Supplementary Table 7.

540

541

542 **Acknowledgments.** We thank Z.G. Cerovic, J.Flexas, F.Morales, and P.Martín for
543 scientific discussions, QuantaLab-IAS-CSIC for laboratory assistance, and G.Altamura,
544 A.Ceglie, and D.Tavano for field support. The study was funded by the European Union's
545 Horizon 2020 research and innovation programme through grant agreements PONTE
546 (635646) and XF-ACTORS (727987). The views expressed are purely those of the writers
547 and may not in any circumstance be regarded as stating an official position of the European
548 Commission.

549

550 **Author contributions.** P.J.Z.-T., C.C., P.S.A.B., B.B.L., D.B., M.S. and J.A.N.-C.
551 designed research; P.J.Z.-T., C.C., P.S.A.B., R.C., A.H., R.H.-C., T.K., M.M.B., L.S.,
552 M.M., V.G.-D., P.R.J.N., B.B.L., D.B., M.S., and J.A.N.-C. performed research; P.J.Z.-T.,
553 C.C., P.S.A.B., R.C., A.H., R.H.-C., T.K., V.G.-D., and J.A.N.-C. analyzed data; and
554 P.J.Z.-T., C.C., P.S.A.B. and J.A.N.-C. wrote the paper. All authors provided comments,
555 read, and approved the final submission.

556

557 **Data and code availability.** The data and the custom code required for the analysis
558 conducted in this study are available at the GitHub repository, address:
559 <https://github.com/Quantalab/Xf-NPlants-2018>

560

561

562 **References**

- 563 1. Paini, D. R. *et al.* Global threat to agriculture from invasive species. *Proc. Natl. Acad. Sci.* **113**, 7575–7579 (2016).
- 564 2. Boyd, L. A., Ridout, C., O'Sullivan, D. M., Leach, J. E. & Leung, H. Plant-pathogen
565 interactions: disease resistance in modern agriculture. *Trends Genet. TIG* **29**, 233–240
566 (2013).
- 567 3. Fisher, M. C. *et al.* Emerging fungal threats to animal, plant and ecosystem health.
568 *Nature* **484**, 186–194 (2012).
- 569 4. Flood, J. The importance of plant health to food security. *Food Secur.* **2**, 215–231
570 (2010).
- 571 5. Strange, R. N. & Scott, P. R. Plant disease: a threat to global food security. *Annu. Rev. Phytopathol.* **43**, 83–116 (2005).
- 572
- 573

- 574 6. Purcell, A. H. *Xylella fastidiosa*, a regional problem or a global threat? *J. Plant Pathol.*
575 **79**, 99–105 (1997).
- 576 7. Stokstad, E. Italy's olives under siege. *Science* **348**, 620–620 (2015).
- 577 8. Almeida, R. P. P. Can Apulia's olive trees be saved? *Science* **353**, 346–348 (2016).
- 578 9. EFSA. The European Union summary report on trends and sources of zoonoses,
579 zoonotic agents and food-borne outbreaks in 2015. *EFSA J.* **14**, (2016).
- 580 10. Hopkins, D. L. & Purcell, A. H. *Xylella fastidiosa*: Cause of Pierce's Disease of
581 Grapevine and Other Emergent Diseases. *Plant Dis.* **86**, 1056–1066 (2002).
- 582 11. *Xylella fastidiosa* World distribution. EPPO Global Database. Available at:
583 <https://gd.eppo.int/taxon/XYLEFA/distribution>. (Accessed: 5th March 2018)
- 584 12. Saponari, M. *et al.* Pilot project on *Xylella fastidiosa* to reduce risk assessment
585 uncertainties. *EFSA Support. Publ.* **13**, n/a-n/a (2016).
- 586 13. Calderón, R., Navas-Cortés, J. A., Lucena, C. & Zarco-Tejada, P. J. High-resolution
587 airborne hyperspectral and thermal imagery for early detection of *Verticillium* wilt of
588 olive using fluorescence, temperature and narrow-band spectral indices. *Remote Sens.*
589 *Environ.* **139**, 231–245 (2013).
- 590 14. Asner, G. P. *et al.* Airborne laser-guided imaging spectroscopy to map forest trait
591 diversity and guide conservation. *Science* **355**, 385–389 (2017).
- 592 15. Harper, S. J., Ward, L. I. & Clover, G. R. G. Development of LAMP and real-time PCR
593 methods for the rapid detection of *Xylella fastidiosa* for quarantine and field
594 applications. *Phytopathology* **100**, 1282–1288 (2010).
- 595 16. Gamon, J. A., Peñuelas, J. & Field, C. B. A narrow-waveband spectral index that tracks
596 diurnal changes in photosynthetic efficiency. *Remote Sens. Environ.* **41**, 35–44 (1992).
- 597 17. Barnes, J. D., Balaguer, L., Manrique, E., Elvira, S. & Davison, A. W. A reappraisal of
598 the use of DMSO for the extraction and determination of chlorophylls a and b in
599 lichens and higher plants. *Environ. Exp. Bot.* **32**, 85–100 (1992).
- 600 18. Peñuelas, J., Filella, I., Lloret, P., Muñoz, F., Vilajeliu, M., Reflectance assessment of
601 mite effects on apple trees. *Int.J.Remote Sen.* **16**, 2727–2733 (1995).
- 602 19. Lev-Yadun, S. & Gould, K. S. Role of Anthocyanins in Plant Defence. in *Anthocyanins*
603 22–28 (Springer, New York, NY, 2008). doi:10.1007/978-0-387-77335-3_2
- 604 20. De La Fuente L, Parker JK, Oliver JE, Granger S, Brannen PM, van Santen E, et al.
605 (2013) The Bacterial Pathogen *Xylella fastidiosa* Affects the Leaf Ionome of Plant
606 Hosts during Infection. PLoS ONE 8(5): e62945.
607 <https://doi.org/10.1371/journal.pone.0062945>
- 608 21. Zeng, W., Melotto, M. & He, S. Y. Plant stomata: a checkpoint of host immunity and
609 pathogen virulence. *Curr. Opin. Biotechnol.* **21**, 599–603 (2010).
- 610 22. Berger, S., Sinha, A. K. & Roitsch, T. Plant physiology meets phytopathology: plant
611 primary metabolism and plant-pathogen interactions. *J. Exp. Bot.* **58**, 4019–4026 (2007).
- 612 23. Tung, J., Goodwin, P. H. & Hsiang, T. Chlorophyll fluorescence for quantification of
613 fungal foliar infection and assessment of the effectiveness of an induced systemic
614 resistance activator. *Eur. J. Plant Pathol.* **136**, 301–315 (2013).
- 615 24. Chaerle, L., Hagenbeek, D., De Bruyne, E., Valcke, R. & Van Der Straeten, D.
616 Thermal and chlorophyll-fluorescence imaging distinguish plant-pathogen interactions
617 at an early stage. *Plant Cell Physiol.* **45**, 887–896 (2004).
- 618 25. Barón, M., Pineda, M. & Pérez-Bueno, M. L. Picturing pathogen infection in plants. *Z.*
619 *Naturforschung C J. Biosci.* **71**, 355–368 (2016).

- 621 26. Giampetruzzi, A. *et al.* Transcriptome profiling of two olive cultivars in response to
622 infection by the CoDiRO strain of *Xylella fastidiosa* subsp. *pauca*. *BMC Genomics* **17**,
623 475 (2016).
- 624 27. Gueymard, C. *SMARTS2: a simple model of the atmospheric radiative transfer of*
625 *sunshine: algorithms and performance assessment*. (Florida Solar Energy Center
626 Cocoa, FL, 1995).
- 627 28. Gueymard, C. A. Parameterized transmittance model for direct beam and circumsolar
628 spectral irradiance. *Sol. Energy* **71**, 325–346 (2001).
- 629 29. Calderón, R., Navas-Cortés, J.A., Zarco-Tejada, P.J. Early Detection and
630 Quantification of Verticillium Wilt in Olive Using Hyperspectral and Thermal Imagery
631 over Large Areas. *Remote Sens.* **7**, 5584–5610 (2015).
- 632 30. Niblack, W. *An Introduction to Digital Image Processing*. (Prentice-Hall, 1986).
- 633 31. Sauvola, J. & Pietikäinen, M. Adaptive document image binarization. *Pattern Recognit.*
634 **33**, 225–236 (2000).
- 635 32. Hartig, S. M. Basic Image Analysis and Manipulation in ImageJ. in *Current Protocols*
636 *in Molecular Biology* (John Wiley & Sons, Inc., 2001).
637 doi:10.1002/0471142727.mb1415s102
- 638 33. Féret, J.-B., Gitelson, A. A., Noble, S. D. & Jacquemoud, S. PROSPECT-D: Towards
639 modeling leaf optical properties through a complete lifecycle. *Remote Sens. Environ.*
640 **193**, 204–215 (2017).
- 641 34. Verhoef, W., Jia, L., Xiao, Q. & Su, Z. Unified Optical-Thermal Four-Stream Radiative
642 Transfer Theory for Homogeneous Vegetation Canopies. *IEEE Trans. Geosci. Remote*
643 *Sens.* **45**, 1808–1822 (2007).
- 644 35. Blackburn, G. A. Wavelet decomposition of hyperspectral data: a novel approach to
645 quantifying pigment concentrations in vegetation. *Int. J. Remote Sens.* **28**, 2831–2855
646 (2007).
- 647 36. Blackburn, G. A. & Ferwerda, J. G. Retrieval of chlorophyll concentration from leaf
648 reflectance spectra using wavelet analysis. *Remote Sens. Environ.* **112**, 1614–1632
649 (2008).
- 650 37. Banskota, A. *et al.* Investigating the Utility of Wavelet Transforms for Inverting a 3-D
651 Radiative Transfer Model Using Hyperspectral Data to Retrieve Forest LAI. *Remote*
652 *Sens.* **5**, 2639–2659 (2013).
- 653 38. Hernández-Clemente, R., North, P. R. J., Hornero, A. & Zarco-Tejada, P. J. Assessing
654 the effects of forest health on sun-induced chlorophyll fluorescence using the
655 FluorFLIGHT 3-D radiative transfer model to account for forest structure. *Remote*
656 *Sens. Environ.* **193**, 165–179 (2017).
- 657 39. Vilfan, N., Tol, C., Muller, O., Rascher, U. & Verhoef, W. *Fluspect-B: A model for leaf*
658 *fluorescence, reflectance and transmittance spectra*. **186**, (2016).
- 659 40. North, P. R. J. Three-dimensional forest light interaction model using a Monte Carlo
660 method. *IEEE Trans. Geosci. Remote Sens.* **34**, 946–956 (1996).
- 661 41. North, P. R. J., Rosette, J. A. B., Suárez, J. C. & Los, S. O. A Monte Carlo radiative
662 transfer model of satellite waveform LiDAR. *Int. J. Remote Sens.* **31**, 1343–1358
663 (2010).
- 664 42. Jacquemoud, S. & Baret, F. PROSPECT: A model of leaf optical properties spectra.
665 *Remote Sens. Environ.* **34**, 75–91 (1990).
- 666 43. Verhoef, W. Light scattering by leaf layers with application to canopy reflectance
667 modeling: The SAIL model. *Remote Sens. Environ.* **16**, 125–141 (1984).

- 668 44. Khattree, R. & Naik, D. N. *Multivariate Data Reduction and Discrimination with SAS*
669 *Software*. (Wiley-SAS, 2000).
- 670 45. Meyer, D. *et al.* *e1071: Misc Functions of the Department of Statistics, Probability*
671 *Theory Group (Formerly: E1071), TU Wien*. (2017).
- 672 46. Ripley, B. & Venables, W. *nnet: Feed-Forward Neural Networks and Multinomial*
673 *Log-Linear Models*. (2016).
- 674 47. Wing, M. K. C. from J. *et al.* *caret: Classification and Regression Training*. (2017).
- 675 48. Richards, J. A. *Remote Sensing Digital Image Analysis*. (1999).
- 676